

A minimal empirical model for the cosmic far-infrared background anisotropies

Hao-Yi Wu^{1,2*} and Olivier Doré^{1,2}

¹California Institute of Technology, 1200 E. California Blvd., MC 367-17, Pasadena, CA 91125, USA

²Jet Propulsion Laboratory, California Institute of Technology, 4800 Oak Grove Drive, Pasadena, CA 91109, USA

Accepted 2017 January 4. Received 2016 December 30; in original form 2016 November 22

ABSTRACT

Cosmic far-infrared background (CFIRB) probes unresolved dusty star-forming galaxies across cosmic time and is complementary to ultraviolet and optical observations of galaxy evolution. In this work, we interpret the observed CFIRB anisotropies using an empirical model based on resolved galaxies in ultraviolet and optical surveys. Our model includes stellar mass functions, star-forming main sequence, and dust attenuation. We find that the commonly used linear Kennicutt relation between infrared luminosity and star formation rate overproduces the observed CFIRB amplitudes. The observed CFIRB requires that low-mass galaxies have lower infrared luminosities than expected from the Kennicutt relation, implying that low-mass galaxies have lower dust content and weaker dust attenuation. Our results demonstrate that CFIRB not only provides a stringent consistency check for galaxy evolution models but also constrains the dust content of low-mass galaxies.

Key words: galaxies: haloes – galaxies: star formation – submillimetre: diffuse background – submillimetre: galaxies

1 INTRODUCTION

Cosmic far-infrared background (CFIRB) originates from unresolved dusty star-forming galaxies from all redshifts and accounts for half of the extragalactic background light generated by galaxies. In dusty star-forming galaxies, $\sim 90\%$ of the ultraviolet (UV) photons produced by recent star-forming activities are absorbed by interstellar dust and re-emitted in far-infrared (FIR; also known as submillimetre, hereafter submm; 100–1000 μm). The FIR luminosities of galaxies are thus tracers of star formation rate (SFR) and are complementary to UV luminosities (e.g., Kennicutt 1998; Kennicutt & Evans 2012; Madau & Dickinson 2014). Compared with UV, galaxies are much less understood in FIR/submm due to the low-resolution of telescopes in these wavelengths. Despite the recent progress in resolving galaxies in FIR/submm (e.g., Casey et al. 2014; Lutz 2014; Dunlop et al. 2017; Fujimoto et al. 2016; Geach et al. 2016), most of the dusty star-forming galaxies remain unresolved. Therefore, CFIRB provides a rare opportunity to study dusty star-forming galaxies under the current resolution limit.

First predicted by Partridge & Peebles (1967) and Bond et al. (1986), CFIRB was discovered by COBE-FIRAS, which also provided to date the only absolute intensity measurement of CFIRB (Puget et al. 1996; Fixsen et al. 1998;

Hauser et al. 1998; Gispert et al. 2000; Hauser & Dwek 2001). Thereafter, the anisotropies of CFIRB have been measured to ever-improving accuracy by *Spitzer* (Lagache et al. 2007), BLAST (Viero et al. 2009), SPT (Hall et al. 2010), *AKARI* (Matsuura et al. 2011), ACT (Hajian et al. 2012), *Herschel*-SPIRE (Amblard et al. 2011; Berta et al. 2011; Viero et al. 2013), and *Planck*-HFI (Planck Collaboration XVIII 2011; Planck Collaboration XXX 2014). In addition, CFIRB maps have been cross-correlated with the lensing potential observed using cosmic microwave background (CMB, Planck Collaboration XVIII 2014) and with near-infrared background (Thacker et al. 2015).

The CFIRB anisotropies have been interpreted mostly using phenomenological models (e.g., Viero et al. 2009; Amblard et al. 2011; Planck Collaboration XVIII 2011; De Bernardis & Cooray 2012; Shang et al. 2012; Xia et al. 2012; Addison et al. 2013; Viero et al. 2013; Planck Collaboration XXX 2014). Although these models can fit the data, they provide limited insight into the underlying galaxy evolution processes. Since galaxy evolution has been extensively studied by UV/optical surveys, it is necessary to understand whether CFIRB agrees with the current knowledge of galaxy evolution.

In this work, we construct an empirical model for dusty star-forming galaxies based on recent galaxy survey results, including stellar mass functions, star-forming main sequence, and dust attenuation. We find that, without in-

* E-mail: hywu@caltech.edu

roducing new parameters, a minimal model can well reproduce the observed CFIRB anisotropies and submm number counts. Our model is the first step towards constructing a comprehensive model for UV, optical, and FIR observations, as well as building multiwavelength mock catalogues for these observations. Such a model is essential for the understanding of cosmic star-formation history and for extracting the most information from multiwavelength surveys.

Our approach is similar to the empirical approach adopted by Béthermin et al. (2012a) and Béthermin et al. (2012c, 2013). Our major innovations include using an N -body simulation and recent self-consistent compilations of stellar mass functions and star-forming main sequence. We also adopt a minimalist approach; that is, we look for the simplest, observationally-motivated model that agrees with CFIRB observations. In each step of our modelling, we directly use constraints from recent observations and avoid introducing new parameters or fitting model to the data. This work is complementary to our earlier work of interpreting CFIRB using a physical gas regulator model (Wu et al. 2016).

This paper is organized as follows. We introduce our model in Section 2 and calculate the CFIRB anisotropies in Section 3. Section 4 compares our model predictions with the observational results of *Planck* and *Herschel*. We discuss our results in Section 5 and summarize in Section 6. Throughout this work, we use the cosmological parameters adopted by the Bolshoi–Planck simulation (see Section 2.1), the stellar population synthesis (SPS) model from Bruzual & Charlot (2003, BC03), and the initial mass function (IMF) from Kroupa (2001).

2 EMPIRICAL MODEL

We construct a model to generate the infrared (IR) spectral flux densities S_ν for a population of galaxies. Our model includes following five steps:

- (i) Sampling dark matter haloes from the Bolshoi–Planck simulation (Section 2.1)
- (ii) Performing abundance matching to assign stellar mass (M_*) to haloes (Section 2.2)
- (iii) Assigning SFR to M_* based on the star-forming main sequence (Section 2.3)
- (iv) Calculating IR luminosity (L_{IR}) based on SFR and M_* (Section 2.4)
- (v) Calculating S_ν by assuming a spectral energy distribution (SED; Section 2.5)

Steps (ii), (iii), and (iv) are demonstrated in Figure 1. Below we describe each step in detail.

2.1 Dark matter haloes from the Bolshoi–Planck simulation

We use the public halo catalogues of the Bolshoi–Planck simulation (Klypin et al. 2016; Rodríguez-Puebla et al. 2016)¹, which is based on a Lambda cold dark matter cosmology

consistent with the *Planck* 2013 results (Planck Collaboration XVI 2014): $\Omega_\Lambda = 0.693$; $\Omega_M = 0.307$; $\Omega_b = 0.048$; $h = 0.678$; $n_s = 0.96$; and $\sigma_8 = 0.823$. The simulation has a box size of $250 h^{-1}\text{Mpc}$ and a mass resolution of $1.5 \times 10^8 h^{-1} M_\odot$.

The simulation is processed with ROCKSTAR halo finder (Behroozi et al. 2013a) and CONSISTENT TREES (Behroozi et al. 2013b). Therefore, the halo catalogues include the mapping between central haloes and subhaloes, as well as the peak circular velocity of a halo in its history (v_{peak}). In this work, we use all haloes with $v_{\text{peak}} > 100 \text{ km s}^{-1}$ between $z = 0.25$ and 5, with a redshift interval of $\Delta z \approx 0.25$. When calculating theoretical uncertainties (see Section 4), we use 0.1% of the haloes in the simulation (~ 6000 haloes in the $z = 0.25$ snapshot) to facilitate the calculation.

2.2 Stellar mass from abundance matching

To assign a stellar mass to each halo, we perform abundance matching between v_{peak} and observed stellar mass functions. The basic concept of abundance matching is to assign higher stellar masses to more massive haloes based on the number density, either monotonically or with some scatter (e.g., Vale & Ostriker 2004; Shankar et al. 2006; Behroozi et al. 2013c; Moster et al. 2013). Instead of halo mass, we use v_{peak} , which is less affected by mass stripping and better correlated with stellar mass (e.g., Nagai & Kravtsov 2005; Conroy et al. 2006; Wang et al. 2006; Wetzel & White 2010; Reddick et al. 2013).

First, we collect observed stellar mass functions from the literature. For $z \leq 3$, we use the recent compilation of stellar mass functions by Henriques et al. (2015, see their figures 2 and A1)², which are calibrated with the *Planck* cosmology. Following Henriques et al. (2015), we add $\Delta M_* = 0.14$ to convert to the BC03 SPS model. For $z \geq 4$, we use the stellar mass functions by Song et al. (2016, see their table 2), which are derived from the rest-frame UV observations from CANDELS, GOODS, and HUDF, based on the BC03 SPS model.

Secondly, we fit the stellar mass functions using redshift-dependent Schechter functions (see Appendix A). For $0 \leq z \leq 3.5$, we use a double Schechter function with constant faint-end slopes; for $3.5 < z \leq 6$, we use a single Schechter function with a time-dependent slope. Using the fitting functions presented in Appendix A, we are able to interpolate smoothly between redshifts. The left-hand panel of Figure 1 shows the data points and the fitting functions. Although we fit the stellar mass function out to $z = 6$, we only use galaxies at $z \leq 5$ in our calculations.

Thirdly, we perform abundance matching between the stellar mass functions and the v_{peak} of haloes, assuming a scatter of 0.2 dex (e.g., Reddick et al. 2013). In the calculation, the input stellar mass function is first deconvolved with the scatter, and then the deconvolved stellar mass function is used to assign M_* to v_{peak} monotonically. We use the code provided by Y.-Y. Mao³, which follows the implementation in Behroozi et al. (2010, 2013c). With this step, a stellar mass is assigned to each halo.

² The data sets are publicly available at http://galformod.mpa-garching.mpg.de/public/LGalaxies/figures_and_data.php.

³ <https://bitbucket.org/yymao/abundancematching>

¹ <http://hipacc.ucsc.edu/Bolshoi/MergerTrees.html>

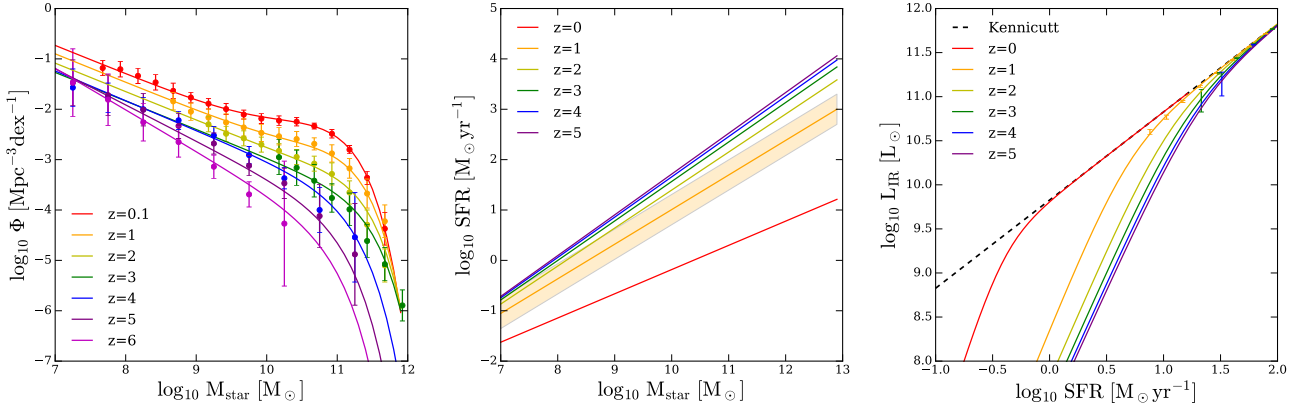


Figure 1. Key elements of our model. Left-hand panel: stellar mass functions from [Henriques et al. \(2015\)](#) and [Song et al. \(2016\)](#). We fit redshift-dependent Schechter functions to the data and perform abundance matching between M_* and v_{peak} (see Section 2.2 and Appendix A). Centre: star-forming main sequence from [Speagle et al. \(2014\)](#), which is used to assign SFR to M_* (see Section 2.3). Right-hand panel: L_{IR} –SFR relation based on the IRX– M_* relation from [Heinis et al. \(2014\)](#). The dashed line corresponds to $L_{\text{IR}} \propto \text{SFR}$ (the Kennicutt relation), which predicts too high L_{IR} for low-mass galaxies (see Section 2.4).

2.3 SFR from the star-forming main sequence

We assign an SFR to each M_* based on the star-forming main sequence compiled by [Speagle et al. \(2014\)](#):

$$\log_{10} \text{SFR}(M_*, t) = (0.84 - 0.026 \times t) \log_{10} M_* - (6.51 - 0.11 \times t), \quad (1)$$

where t is the age of the universe in Gyr. This relation is shown in the central panel of Figure 1. The compilation of [Speagle et al. \(2014\)](#) is based on the Kroupa IMF, the BC03 SPS model, and the cosmological parameters $\Omega_\Lambda = 0.7$, $\Omega_M = 0.3$, and $h = 0.7$. This cosmology is slightly different from our choice; however, these authors stated that the effect of cosmology is negligible for the main-sequence calibration.

In our calculation, for each $\log_{10} M_*$, an SFR is drawn from a normal distribution with a mean given by the equation above and a scatter of 0.3 dex. We note that [Speagle et al. \(2014\)](#) have shown that the intrinsic scatter (deconvolved with the evolution in a redshift bin) and the true scatter (excluding observational uncertainties) of the main sequence are 0.3 and 0.2 dex, respectively. We find that a scatter of 0.2 dex produces too low number counts and too low shot noise (see Section 4). In the central panel of Figure 1, we show a 0.3 dex of scatter around the mean relation at $z = 1$.

2.4 Infrared luminosity from SFR and stellar mass

To calculate L_{IR} , it is commonly assumed that $L_{\text{IR}} \propto \text{SFR}$ (the Kennicutt relation; [Kennicutt 1998](#); [Kennicutt & Evans 2012](#)). However, this relation is known to break down for low-mass galaxies, which tend to have lower dust content, lower attenuation, and lower L_{IR} (e.g., [Pannella et al. 2009](#); [Garn & Best 2010](#); [Buat et al. 2012](#); [Hayward et al. 2014](#)). One way to improve upon the Kennicutt relation is to assume that the photons produced by star formation are split into UV and IR,

$$\text{SFR} = K_{\text{UV}} L_{\text{UV}} + K_{\text{IR}} L_{\text{IR}}, \quad (2)$$

and then use a relation between L_{IR} and L_{UV} (e.g., [Bernhard et al. 2014](#)). The logarithm of the ratio between L_{IR} and L_{UV}

is commonly referred to as the IR-excess (IRX),

$$\text{IRX} = \log_{10} \left(\frac{L_{\text{IR}}}{L_{\text{UV}}} \right), \quad (3)$$

and has been calibrated observationally. Given the two equations above, we can solve for L_{IR} :

$$L_{\text{IR}} = \frac{\text{SFR}}{K_{\text{IR}} + K_{\text{UV}} 10^{-\text{IRX}(M_*)}}. \quad (4)$$

We use $K_{\text{UV}} = 1.71 \times 10^{-10}$ and $K_{\text{IR}} = 1.49 \times 10^{-10}$ from [Kennicutt & Evans \(2012\)](#) based on the Kroupa IMF.

[Heinis et al. \(2014\)](#) calibrated the IRX–stellar mass relation based on the rest-frame UV-selected galaxies at $z \sim 1.5, 3,$ and 4 in the COSMOS field observed with *Herschel*-SPIRE (part of the HerMES program). They provided the fitting function

$$\text{IRX}(M_*) = \alpha \log_{10} \left(\frac{M_*}{10^{10.35} M_\odot} \right) + \text{IRX}_0, \quad (5)$$

where $\text{IRX}_0 = 1.32$ and $\alpha = 0.72$. We adopt $\alpha = 1.5$, which agrees better with the CFIRB amplitudes and is still consistent with their observations (see below).

The right-hand panel of Figure 1 demonstrates the L_{IR} –SFR relation with this $\text{IRX}(M_*)$, which produces lower L_{IR} for low-SFR galaxies compared with the Kennicutt relation ([Kennicutt & Evans 2012](#), the dashed line). We show the data points from [Heinis et al. \(2014\)](#) to demonstrate the level of uncertainties in observations. In particular, we use the M_* and IRX from their figure 3 and calculate the corresponding SFR and L_{IR} . We note that the current observations can only constrain the brightest end, and we need to extrapolate to the faint end. As we will discuss in Section 4.1, this mass-dependent attenuation is essential for reproducing the observed CFIRB amplitudes.

2.5 Spectral energy distribution

With the L_{IR} calculated above, we need the SED Θ_ν to calculate the spectral flux density S_ν . The spectral luminosity density is given by

$$L_\nu = L_{\text{IR}} \Theta_\nu, \quad (6)$$

and S_ν at the observed frequency ν is given by

$$S_\nu = \frac{L_{(1+z)\nu}}{4\pi\chi^2(1+z)}, \quad (7)$$

where χ is the comoving distance, and $L_{(1+z)\nu}$ is evaluated at the rest-frame frequency $(1+z)\nu$.

We assume that the SED of each galaxy is given by a single-temperature modified blackbody,

$$\Theta_\nu \propto \nu^\beta B_\nu(T_d), \quad (8)$$

where B_ν is the Planck function, T_d is the dust temperature, and β is the spectral index. The SED is normalized such that $\int d\nu\Theta_\nu = 1$. We adopt $\beta = 2.1$ based on our previous work for CFIRB (Wu et al. 2016), and we note that $\beta = 2$ is widely used and theoretically motivated (Draine & Lee 1984; Mathis & Whiffen 1989).

To calculate the T_d of each galaxy, we adopt the relation between T_d and specific star formation rate (SSFR, SFR/ M_*) given by Magnelli et al. (2014),

$$T_d = 98 [K] \times (1+z)^{-0.065} + 6.9 \log_{10} \text{SSFR}, \quad (9)$$

and we assume a normal distribution with a scatter of 2 K around this relation (consistent with their figure 10). This relation is derived from galaxies up to $z \sim 2$ from the PEP and HerMES programs of *Herschel* with multiwavelength observations. The stellar mass is derived from SED fitting, while the SFR is derived by combining UV and IR. These authors bin galaxies based on SFR, M_* , and z and calculate T_d using the stacked far-infrared flux density in each bin. They have found that the T_d -SSFR relation is tighter than the T_d - L_{IR} relation.

3 CALCULATING THE CFIRB ANGULAR POWER SPECTRA

With the prediction of S_ν for each halo in the catalogues, we proceed to compute the CFIRB angular power spectra. The formalism presented below is motivated by the analytical halo model presented in Shang et al. (2012), and we make various generalization and adjustments for our sampling approach. Since we use subhaloes from an N -body simulation, we expect our approach to be more accurate than a purely analytical calculation.

The CFIRB auto angular power spectrum is given by the sum of the two-halo term, the one-halo term, and the shot noise:

$$C_\ell^\nu = C_\ell^{\nu,2\text{h}} + C_\ell^{\nu,1\text{h}} + C_\ell^{\nu,\text{shot}}. \quad (10)$$

Here we present the equations for a single frequency; the equations for two-frequency cross-spectra can be generalized easily.

The two-halo term corresponds to the contribution from two galaxies in distinct haloes and is given by

$$C_\ell^{\nu,2\text{h}} = \int \chi^2 d\chi F_\nu^2(z) P_{\text{lin}} \left(k = \frac{\ell}{\chi}, z \right), \quad (11)$$

where $P_{\text{lin}}(k, z)$ is the linear matter power spectrum calculated with CAMB (Lewis et al. 2000), and

$$F_\nu(z) = \int dM \frac{dn}{dM} b(M) \left(S_\nu^{\text{cen}} + \int dM_s \frac{dN(M)}{dM_s} S_\nu^{\text{sat}} \right),$$

where M is the mass of central haloes, dn/dM and $b(M)$ are the mass function and halo bias of central haloes, M_s is the mass of subhaloes, and $dN(M)/dM_s$ is the number of subhaloes in a central halo. In our sampling approach, the integration is replaced by the sum over all $b(M)S_\nu$, and for a satellite galaxy we use the $b(M)$ of its central halo. For $b(M)$, we use the fitting function of halo bias from Tinker et al. (2010), and we have verified that this fitting function agrees with the linear halo bias measured directly from the Bolshoi-Planck simulation.

The one-halo term corresponds to the contribution from two galaxies in the same halo and is given by

$$C_\ell^{\nu,1\text{h}} = \int \chi^2 d\chi G_\nu(k = \ell/\chi, z), \quad (13)$$

where

$$G_\nu(k, z) = 2 \int dM \frac{dn}{dM} S_\nu^{\text{cen}} \left(\int dM_s \frac{dN(M)}{dM_s} S_\nu^{\text{sat}} \right) u(k, z) + \int dM \frac{dn}{dM} \left(\int dM_s \frac{dN(M)}{dM_s} S_\nu^{\text{sat}} \right)^2 u^2(k, z). \quad (14)$$

Here, $u(k, z)$ is the density profile of dark matter haloes in the Fourier space, and $u(k, z) \approx 1$ for the large scales discussed in this work. The first term corresponds to summing over the central-satellite pairs in a halo, and the second term corresponds to summing over the satellite-satellite pairs in a halo. We avoid self-pairs in calculating the second term.

The shot noise corresponds to self-pairs of galaxies and is given by

$$C_\ell^{\nu,\text{shot}} = \int \chi^2 d\chi \int dS_\nu \frac{dn}{dS_\nu} S_\nu^2, \quad (15)$$

where S_ν includes both central and satellite galaxies.

The cross angular spectrum between CFIRB and CMB lensing potential is given by

$$C_\ell^{\phi\nu} = \int_0^{\chi_*} \chi^2 d\chi (1+z) F_\nu(z) \frac{3}{\ell^2} \Omega_M H_0^2 \left(\frac{\chi_* - \chi}{\chi_* \chi} \right) \times P_{\text{lin}} \left(k = \frac{\ell}{\chi}, z \right), \quad (16)$$

where χ_* is the comoving distance to the last-scattering surface, and $F_\nu(z)$ is given by Equation 12.

4 COMPARISON WITH OBSERVATIONS

In this section we compare our model predictions with observational results.

4.1 CFIRB anisotropies

We compare our model with the CFIRB anisotropies observed by *Planck*:

- [Planck Collaboration XXX \(2014\)](#) presents the CFIRB observed by *Planck*-HFI for an area of 2240 deg², for which HI maps are available for removing the foreground Galactic dust emission. The primordial CMB, the Sunyaev-Zeldovich effect, and the radio sources are also removed. We compare

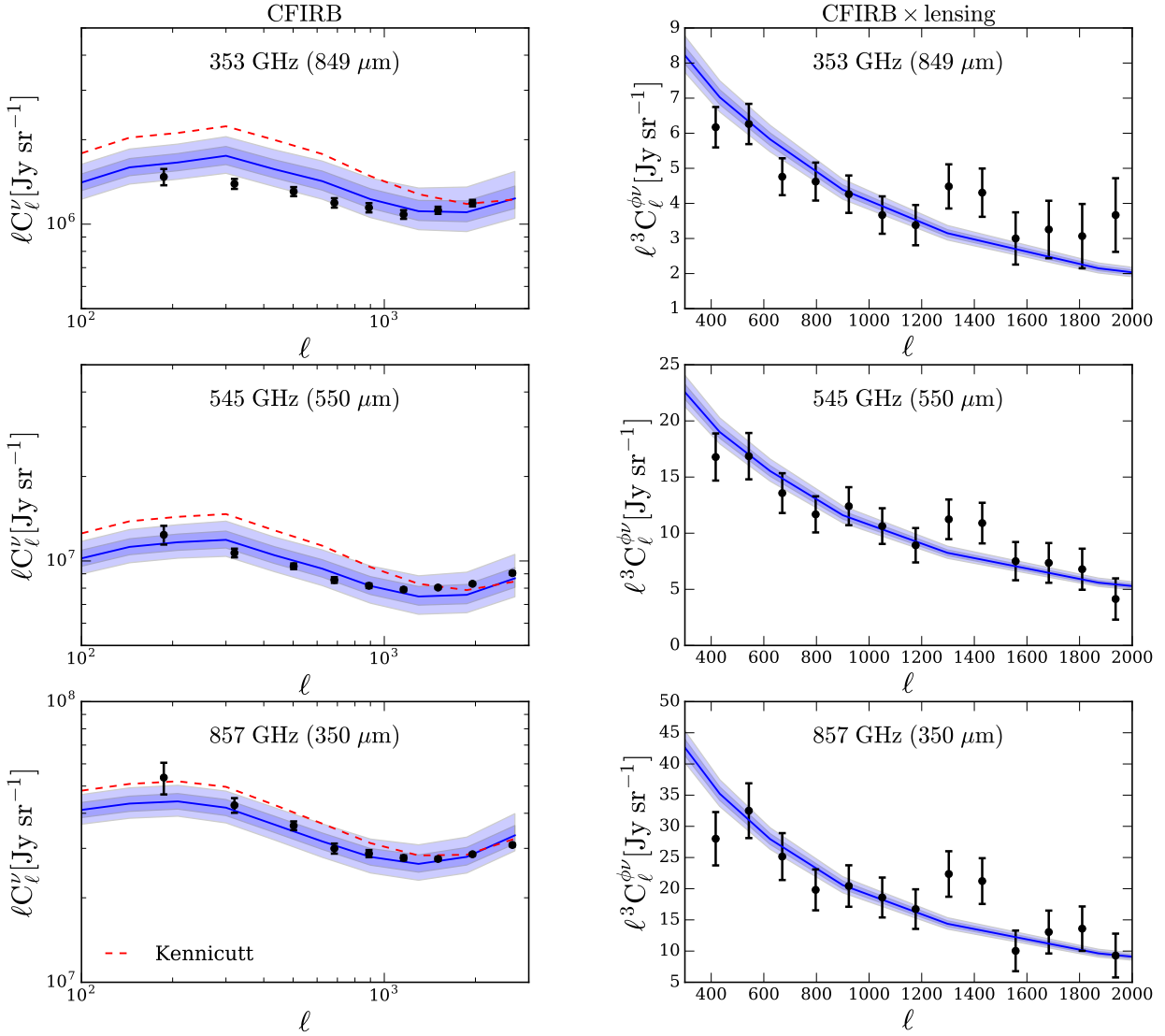


Figure 2. Comparison between our model (blue bands) and the CFIRB anisotropies observed by *Planck* (data points). Left-hand panel: CFIRB auto angular power spectra from [Planck Collaboration XXX \(2014\)](#). The red dashed curves show that the Kennicutt relation overproduces the large-scale amplitudes. Right-hand panel: cross-angular power spectra between CFIRB and CMB lensing potential from [Planck Collaboration XVIII \(2014\)](#). The dark and light blue bands correspond to the 68% and 95% intervals of theoretical uncertainties, respectively.

our model with the CFIRB angular power spectra for $187 \leq \ell \leq 2649$, presented in their table D.2.

- [Planck Collaboration XVIII \(2014\)](#) presents the first detection of the cross-correlation between CFIRB and CMB lensing potential (the latter is extracted from the low-frequency bands of *Planck*). The CMB lensing potential is dominated by dark matter haloes between $z \approx 1$ and 3, and CFIRB is dominated by galaxies in the same redshift range; therefore, the cross-correlation between CFIRB and CMB lensing potential directly probes the connection between FIR galaxies and dark matter haloes. In addition, compared with the auto-correlation of CFIRB, this cross-correlation is less affected by the contamination of Galactic dust.

Figure 2 compares our model predictions with the ob-

servational results described above. We include the results in 353, 545, and 857 GHz (849, 550, and 350 μm), and we exclude 217 GHz because CMB dominates this band for all angular scales. In all calculations, we apply the colour-correction factors and flux cuts of [Planck Collaboration XXX \(2014, see their section 5.3 and table 1\)](#). The left column corresponds to the auto angular power spectra of CFIRB, C_ℓ^ν , while the right column corresponds to the cross-angular power spectra between CFIRB and CMB lensing potential, $C_\ell^{\phi\nu}$. To calculate the theoretical uncertainties, we repeat Steps (iii) to (v) in Section 2 for 1000 times, and we use 0.1% of the haloes in the Bolshoi–Planck simulation to facilitate the calculation. The dark and light blue bands correspond to the 68% and 95% intervals of the theoretical uncertainties. As can be seen, our model well captures both observational

results. We emphasize that we perform no fitting to the data, and that all the components of our model directly come from independent surveys of UV, optical, and FIR.

The red dashed curves in the left column of Figure 2 show that, if we assume the Kennicutt relation ($L_{\text{IR}} \propto \text{SFR}$) instead of the mass-dependent dust attenuation, we produce too high large-scale amplitudes of the power spectra. The Kennicutt relation assigns too high L_{IR} to low-mass galaxies, and because of the high number density of low-mass galaxies, it leads to too high CFIRB large-scale amplitudes. In this sense, CFIRB can be used to constrain the SFR and dust content of low-mass galaxies. We note that the Kennicutt relation and the mass-dependent attenuation produce very similar small-scale power spectra. The reason is that the two models have very similar L_{IR} for massive galaxies, and the small-scale spectra are dominated by shot noise, which is contributed mostly by massive galaxies.

4.2 Number counts

In this section, we turn to submm number counts, which are dominated by massive galaxies. We compare our model with the number counts observed by *Herschel*-SPIRE at 250, 350, and 500 μm (1200, 857, and 600 GHz):

- Béthermin et al. (2012b) presented the deep number counts from the HerMES survey (the COSMOS and GOODS-N fields). They performed stacked analyses based on the 24 μm sources, and they managed to extract the number counts down to ~ 2 mJy.
- Valiante et al. (2016) presented the number counts from the H-ATLAS survey of an area of 161.6 deg^2 (the GAMA fields). At the faint end, their results agree with Béthermin et al. (2012b); at the bright end, they have better statistics due to the larger survey area.

Figure 3 compares the number counts from our model with the two observational results described above. For this calculation, we use all haloes in the Bolshoi–Planck simulation to obtain enough bright galaxies. We note that the observed brightest end ($\gtrsim 100$ mJy) is dominated by gravitationally lensed sources, which we do not have in our model. Our model mostly agrees with the observational results; however, for 250 μm (1200 GHz) our model produces slightly higher number counts; this could result from our oversimplified assumption for SED.

5 DISCUSSIONS

In our model, we assume that all galaxies belong to the star-forming main sequence. This is a simplified assumption, because it is known that a fraction of massive galaxies are quiescent (e.g., Ilbert et al. 2013; Moustakas et al. 2013; Muzzin et al. 2013; Tomczak et al. 2014; Man et al. 2016; Schreiber et al. 2016). In addition, studies have also shown that quiescent galaxies can still have significant FIR emission due to the dust heated by old stars (the so-called cirrus dust emission, e.g., Fumagalli et al. 2014; Hayward et al. 2014; Narayanan et al. 2015). In Wu et al. (2016), we have also found that the observed CFIRB requires substantial FIR emission from massive haloes.

We have attempted to include quiescent galaxies in this

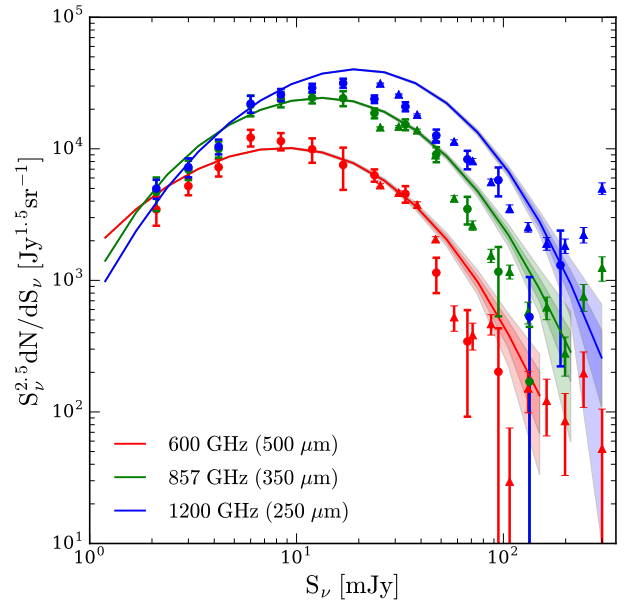


Figure 3. Number counts predicted from our model (colour bands) compared with the results from HerMES (Béthermin et al. 2012b, circles) and H-ATLAS (Valiante et al. 2016, triangles). The dark and light bands correspond to the 68% and 95% intervals of the theoretical uncertainties, respectively.

work, but we find that the CFIRB data cannot distinguish between L_{IR} coming from star formation and cirrus dust. When we include a fraction of quiescent galaxies with $\text{SSFR} = 10^{-12} \text{yr}^{-1}$ (e.g., Muzzin et al. 2013; Fumagalli et al. 2014), the power spectra are lowered, and we need to add cirrus dust emission to these quiescent galaxies to compensate for the lowered power. However, the fraction of quiescent galaxies and the cirrus dust emission are both highly uncertain and degenerate with each other; therefore, we decide not to include them in this work. Investigating the contribution from quiescent galaxies will require the modelling of old stars and cirrus dust, as well as comparisons with near-infrared observations. We will investigate this in future work.

Furthermore, it is also known that a small fraction of galaxies undergo starburst phases and have significantly higher SFR and IR luminosities (e.g., Elbaz et al. 2011). The starburst galaxies account for $\sim 10\%$ of the cosmic SFR density at $z \sim 2$ (Rodighiero et al. 2011; Sargent et al. 2012) and are expected to have negligible contribution to the CFIRB (e.g., Shang et al. 2012; Béthermin et al. 2013). The effect of starburst galaxies will be degenerate with that of quiescent galaxies in producing CFIRB. Therefore, any departure from the star-forming main sequence will require constraints from multiwavelength observations, which will be explored in our future work.

In this work, we choose a minimal number of modelling steps in order to avoid degeneracies. Except for the slope of the $\text{IRX}-M_*$ relation, all the other parameter values are directly taken from the literature, and we neither introduce new parameters nor fit parameters to the data. In our future work, we plan to incorporate more astrophysical processes (including quiescent and starburst galaxies, realistic SEDs) into our model, combine multiwavelength observational results from UV, optical, near-IR, FIR, and radio surveys, and

perform Markov chain Monte Carlo calculations to constrain model parameters,

Over the next decade, new instruments are expected to revolutionize the view of the FIR/submm sky. The Far-infrared Surveyor (Origins Space Telescope), which is currently planned by NASA, prioritizes the measurements of cosmic SFR. The Cosmic Origins Explorer (CORE, De Zotti et al. 2016) and the ground-based CMB-S4 experiment (Abazajian et al. 2016) will measure CFIRB and CMB lensing to unprecedented precision. The Primordial Inflation Explorer (PIXIE, Kogut et al. 2011) will significantly improve the accuracy of the absolute intensity of CFIRB compared with *COBE*-FIRAS. These missions are expected to lead to a consistent picture of cosmic star formation history. In a companion paper, we apply a principle component approach to investigate the optimal experimental designs for constraining the cosmic star-formation history using CFIRB (Wu & Doré 2016). We plan to apply the empirical approach presented in this paper to generate mock catalogues, check consistencies between models, and develop survey strategies for these observational programs.

6 SUMMARY

We present a minimal empirical model for dusty star-forming galaxies to interpret the observations of CFIRB anisotropies and submm number counts. Our model is based on the Bolshoi–Planck simulation and various results from UV/optical/IR galaxy surveys. Below we summarize our model and findings:

- To assign IR spectral flux densities S_ν to dark matter haloes, we model stellar mass (using abundance matching between v_{peak} and observed stellar mass functions), SFR (using the star-forming main sequence), L_{IR} (assuming a mass-dependent attenuation), and SED (assuming a modified blackbody).

- Given the connection between S_ν and halo mass obtained above, we apply an extended halo model to calculate the auto angular power spectra of CFIRB and the cross-angular power spectra between CFIRB and CMB lensing potential. We find that the commonly used Kennicutt relation, $L_{\text{IR}} \propto \text{SFR}$, leads to too high CFIRB amplitudes. The observed CFIRB amplitudes require that low-mass galaxies have lower L_{IR} than expected from the Kennicutt relation. This trend has been observed previously and is related to the low dust content of low-mass galaxies.

- Our model also produces submm number counts that agree with observational results of *Herschel*. The number counts are contributed by massive haloes, and this agreement indicates that our minimal model (star-forming main sequence only, no quiescent or starburst galaxies) is sufficient for dusty star-forming galaxies in massive haloes. We slightly overproduce the number counts at 250 μm (1200 GHz), and this may indicate that the SEDs of dust emission deviate from a simple modified blackbody.

Our results indicate that the observed CFIRB broadly agrees with the current knowledge of galaxy evolution from resolved galaxies in UV and optical surveys, under the assumption that low-mass galaxies produces IR luminosities

lower than expected from the Kennicutt relation. Therefore, CFIRB provides a rare opportunity of constraining the SFR and dust production in low-mass galaxies. However, since CFIRB does not provide redshifts of galaxies, further investigations for low-mass galaxies will require the cross-correlation between CFIRB with galaxies or extragalactic background light observed in other wavelengths (e.g., Cooray 2016; Serra et al. 2016).

ACKNOWLEDGEMENTS

We thank Joanne Cohn and Martin White for helpful discussions, and we thank Yao-Yuan Mao for providing the code and assistance for the abundance matching calculation. HW acknowledges the support by the US National Science Foundation (NSF) grant AST1313037. The calculations in this work were performed on the Caltech computer cluster Zwicky, which is supported by NSF MRI-R2 award number PHY-096029. OD acknowledges the hospitality of the Aspen Center for Physics, which is supported by NSF grant PHY-1066293. Part of the research described in this paper was carried out at the Jet Propulsion Laboratory, California Institute of Technology, under a contract with the National Aeronautics and Space Administration. The Bolshoi–Planck simulation was performed by Anatoly Klypin within the Bolshoi project of the University of California High-Performance AstroComputing Center (UC-HiPACC) and was run on the Pleiades supercomputer at the NASA Ames Research Center.

REFERENCES

- Abazajian K. N., et al., 2016, preprint, ([arXiv:1610.02743](https://arxiv.org/abs/1610.02743))
- Addison G. E., Dunkley J., Bond J. R., 2013, *MNRAS*, **436**, 1896
- Amblard A., et al., 2011, *Nature*, **470**, 510
- Behroozi P. S., Conroy C., Wechsler R. H., 2010, *ApJ*, **717**, 379
- Behroozi P. S., Wechsler R. H., Wu H.-Y., 2013a, *ApJ*, **762**, 109
- Behroozi P. S., Wechsler R. H., Wu H.-Y., Busha M. T., Klypin A. A., Primack J. R., 2013b, *ApJ*, **763**, 18
- Behroozi P. S., Wechsler R. H., Conroy C., 2013c, *ApJ*, **770**, 57
- Bernhard E., Béthermin M., Sargent M., Buat V., Mullaney J. R., Pannella M., Heinis S., Daddi E., 2014, *MNRAS*, **442**, 509
- Berta S., et al., 2011, *A&A*, **532**, A49
- Béthermin M., Doré O., Lagache G., 2012a, *A&A*, **537**, L5
- Béthermin M., et al., 2012b, *A&A*, **542**, A58
- Béthermin M., et al., 2012c, *ApJ*, **757**, L23
- Béthermin M., Wang L., Doré O., Lagache G., Sargent M., Daddi E., Cousin M., Aussel H., 2013, *A&A*, **557**, A66
- Bond J. R., Carr B. J., Hogan C. J., 1986, *ApJ*, **306**, 428
- Bruzual G., Charlot S., 2003, *MNRAS*, **344**, 1000
- Buat V., et al., 2012, *A&A*, **545**, A141
- Casey C. M., Narayanan D., Cooray A., 2014, *Phys. Rep.*, **541**, 45
- Conroy C., Wechsler R. H., Kravtsov A. V., 2006, *ApJ*, **647**, 201
- Cooray A., 2016, *R. Soc. Open Sci.*, **3**, 150555
- De Bernardis F., Cooray A., 2012, *ApJ*, **760**, 14
- De Zotti G., et al., 2016, preprint, ([arXiv:1609.07263](https://arxiv.org/abs/1609.07263))
- Draine B. T., Lee H. M., 1984, *ApJ*, **285**, 89
- Dunlop J. S., et al., 2017, *MNRAS*, **466**, 861
- Elbaz D., et al., 2011, *A&A*, **533**, A119
- Fixsen D. J., Dwek E., Mather J. C., Bennett C. L., Shafer R. A., 1998, *ApJ*, **508**, 123
- Fujimoto S., Ouchi M., Ono Y., Shibuya T., Ishigaki M., Nagai H., Momose R., 2016, *ApJS*, **222**, 1
- Fumagalli M., et al., 2014, *ApJ*, **796**, 35

Garn T., Best P. N., 2010, *MNRAS*, **409**, 421
 Geach J. E., Dunlop J. S., Halpern M., et al., 2016, preprint, ([arXiv:1607.03904](#))
 Gispert R., Lagache G., Puget J. L., 2000, *A&A*, **360**, 1
 Hajian A., et al., 2012, *ApJ*, **744**, 40
 Hall N. R., et al., 2010, *ApJ*, **718**, 632
 Hauser M. G., Dwek E., 2001, *ARA&A*, **39**, 249
 Hauser M. G., et al., 1998, *ApJ*, **508**, 25
 Hayward C. C., et al., 2014, *MNRAS*, **445**, 1598
 Heinis S., et al., 2014, *MNRAS*, **437**, 1268
 Henriques B. M. B., White S. D. M., Thomas P. A., Angulo R., Guo Q., Lemson G., Springel V., Overzier R., 2015, *MNRAS*, **451**, 2663
 Ilbert O., et al., 2013, *A&A*, **556**, A55
 Kennicutt Jr. R. C., 1998, *ApJ*, **498**, 541
 Kennicutt R. C., Evans N. J., 2012, *ARA&A*, **50**, 531
 Klypin A., Yepes G., Gottlöber S., Prada F., Heß S., 2016, *MNRAS*, **457**, 4340
 Kogut A., et al., 2011, *J. Cosmol. Astropart. Phys.*, **7**, 25
 Kroupa P., 2001, *MNRAS*, **322**, 231
 Lagache G., Bavouzet N., Fernandez-Conde N., Ponthieu N., Rodet T., Dole H., Miville-Deschênes M.-A., Puget J.-L., 2007, *ApJ*, **665**, L89
 Lewis A., Challinor A., Lasenby A., 2000, *ApJ*, **538**, 473
 Lutz D., 2014, *ARA&A*, **52**, 373
 Madau P., Dickinson M., 2014, *ARA&A*, **52**, 415
 Magnelli B., et al., 2014, *A&A*, **561**, A86
 Man A. W. S., et al., 2016, *ApJ*, **820**, 11
 Mathis J. S., Whiffen G., 1989, *ApJ*, **341**, 808
 Matsuura S., et al., 2011, *ApJ*, **737**, 2
 Moster B. P., Naab T., White S. D. M., 2013, *MNRAS*, **428**, 3121
 Moustakas J., et al., 2013, *ApJ*, **767**, 50
 Muzzin A., et al., 2013, *ApJ*, **777**, 18
 Nagai D., Kravtsov A. V., 2005, *ApJ*, **618**, 557
 Narayanan D., et al., 2015, *Nature*, **525**, 496
 Pannella M., et al., 2009, *ApJ*, **698**, L116
 Partridge R. B., Peebles P. J. E., 1967, *ApJ*, **148**, 377
 Planck Collaboration XVI 2014, *A&A*, **571**, A16
 Planck Collaboration XVIII 2011, *A&A*, **536**, A18
 Planck Collaboration XVIII 2014, *A&A*, **571**, A18
 Planck Collaboration XXX 2014, *A&A*, **571**, A30
 Puget J.-L., Abergel A., Bernard J.-P., Boulanger F., Burton W. B., Desert F.-X., Hartmann D., 1996, *A&A*, **308**, L5
 Reddick R. M., Wechsler R. H., Tinker J. L., Behroozi P. S., 2013, *ApJ*, **771**, 30
 Rodighiero G., et al., 2011, *ApJ*, **739**, L40
 Rodríguez-Puebla A., Behroozi P., Primack J., Klypin A., Lee C., Hellinger D., 2016, *MNRAS*, **462**, 893
 Sargent M. T., Béthermin M., Daddi E., Elbaz D., 2012, *ApJ*, **747**, L31
 Schreiber C., Elbaz D., Pannella M., Ciesla L., Wang T., Koelmoer A., Rafelski M., Daddi E., 2016, *A&A*, **589**, A35
 Serra P., Doré O., Lagache G., 2016, *ApJ*, **833**, 153
 Shang C., Haiman Z., Knox L., Oh S. P., 2012, *MNRAS*, **421**, 2832
 Shankar F., Lapi A., Salucci P., De Zotti G., Danese L., 2006, *ApJ*, **643**, 14
 Song M., et al., 2016, *ApJ*, **825**, 5
 Speagle J. S., Steinhardt C. L., Capak P. L., Silverman J. D., 2014, *ApJS*, **214**, 15
 Thacker C., Gong Y., Cooray A., De Bernardis F., Smidt J., Mitchell-Wynne K., 2015, *ApJ*, **811**, 125
 Tinker J. L., Robertson B. E., Kravtsov A. V., Klypin A., Warren M. S., Yepes G., Gottlöber S., 2010, *ApJ*, **724**, 878
 Tomczak A. R., et al., 2014, *ApJ*, **783**, 85
 Vale A., Ostriker J. P., 2004, *MNRAS*, **353**, 189
 Valiante E., et al., 2016, *MNRAS*, **462**, 3146
 Viero M. P., et al., 2009, *ApJ*, **707**, 1766

Viero M. P., et al., 2013, *ApJ*, **772**, 77
 Wang L., Li C., Kauffmann G., De Lucia G., 2006, *MNRAS*, **371**, 537
 Wetzel A. R., White M., 2010, *MNRAS*, **403**, 1072
 Wu H.-Y., Doré O., 2016, preprint, ([arXiv:1612.02474](#))
 Wu H.-Y., Doré O., Teyssier R., 2016, preprint, ([arXiv:1607.02546](#))
 Xia J.-Q., Negrello M., Lapi A., De Zotti G., Danese L., Viel M., 2012, *MNRAS*, **422**, 1324

APPENDIX A: FITTING THE OBSERVED STELLAR MASS FUNCTIONS

In Section 2.2, we fit redshift-dependent Schechter functions to the observed stellar mass functions. We minimize

$$\chi^2 = \frac{\sum (\log_{10} \Phi_{\text{model}} - \log_{10} \Phi_{\text{data}})^2}{(\Delta \log_{10} \Phi_{\text{data}})^2}. \quad (\text{A1})$$

For $0 \leq z \leq 3.5$, we use a double Schechter function:

$$\begin{aligned} \Phi(M_*) &= \frac{dn}{d \log_{10} M_*} [\text{Mpc}^{-3} \text{dex}^{-1}] \\ &= (\Phi_1 m^{1+\alpha_1} + \Phi_2 m^{1+\alpha_2}) e^{-m} \ln(10), \end{aligned} \quad (\text{A2})$$

where

$$m = \frac{M_*}{M_0}. \quad (\text{A3})$$

We assume that M_0 , Φ_1 , and Φ_2 depend on z , while α_1 and α_2 are independent of z . The best-fitting parameters are

$$\begin{aligned} \log_{10} M_0 &= 10.90 + 0.08 \times z \\ \log_{10} \Phi_1 &= -2.4 - 0.61 \times z \\ \log_{10} \Phi_2 &= -3.29 - 0.23 \times z \\ \alpha_1 &= -0.68 \\ \alpha_2 &= -1.57 \end{aligned} \quad (\text{A4})$$

with $\chi^2 = 7.4$ with 41 degrees of freedom.

For $3.5 < z \leq 6$, we use a single Schechter function:

$$\Phi(M_*) = \Phi_1 m^{1+\alpha_1} e^{-m} \ln(10), \quad (\text{A5})$$

and we assume that all parameters depend on $\ln(1+z)$. The best-fitting parameters are

$$\begin{aligned} \log_{10} M_0 &= 12.26 - 0.77 \times \ln(1+z) \\ \log_{10} \Phi_1 &= -0.77 - 1.99 \times \ln(1+z) \\ \alpha_1 &= -0.47 - 0.69 \times \ln(1+z) \end{aligned} \quad (\text{A6})$$

with $\chi^2 = 3.7$ with 19 degrees of freedom. The fitting functions are shown in the left-hand panel of Figure 1.

This paper has been typeset from a $\text{\TeX}/\text{\LaTeX}$ file prepared by the author.